Journal of Structural Geology 31 (2009) 561–574

Contents lists available at ScienceDirect

Journal of Structural Geology

journal homepage: www.elsevier.com/locate/jsg

Anisotropy, pore fluid pressure and low angle normal faults

David Healy*

The Institute for Geoscience Research (TIGeR), Department of Applied Geology, Curtin University of Technology, GPO Box U1987, Perth, Western Australia 6845, Australia

ARTICLE INFO

Article history:
Received 24 November 2008
Received in revised form
16 February 2009
Accepted 3 March 2009
Available online 12 March 2009

Keywords:
Effective Medium Theory
Poroelastic
Fault core
Damage zone
Crack
Effective stress

ABSTRACT

Low angle normal faults (LANFs) are commonly associated with high-angle normal faults, high pore fluid pressures and foliated fault cores. Explanations for LANF slip based on high pore fluid pressure critically depend on stress rotations in the fault core zone, which have been based on an assumption of isotropy. Anisotropy fundamentally changes the coupling between pore fluid pressure and effective stress. The response of saturated fault core rocks in LANFs can be explored by combining the Effective Medium Theory with anisotropic poroelasticity. The nucleation and evolution of LANFs are investigated in a framework of local changes in rock properties and the interaction of a pressurised pore fluid with intrinsic (lithological) and extrinsic (damage) anisotropies. This quantitative approach enables comparison with detailed field and laboratory measurements of fault rock properties.

1. Introduction

1.1. Background

Slip on low angle normal faults (LANFs, dip $< 30°$) is impossible according to the standard fault mechanics (Jaeger et al., 2007) and measured values of rock friction (Byerlee, 1978). Vertical lithostatic loads result in a high value of compressive normal stress acting on the fault plane and for typical coefficients of friction in the range $0.6 < \mu < 0.85$, the fault will be locked. However, some LANFs are seismically active, including examples in the Woodlark Basin of the SW Pacific (Abers, 1991; Abers et al., 1997) and around Corinth in Greece (Rietbrock et al., 1996). Microseismicity has been recorded along the low angle Alto Tiberina fault in the Apennines of central Italy (Chiaraluce et al., 2007).

LANFs can be classified with other 'weak' faults (e.g. San Andreas fault, USA), where the fault plane is oriented at a high angle to the regional maximum compressive stress, σ_1 (Zoback et al., 1987; Townend and Zoback, 2004; in this paper $\sigma_1 > \sigma_2 > \sigma_3$). The physical cause of fault weakness is the subject of vigorous debate. Suggested mechanisms include: inherently weak material in the fault zone (Wang et al., 1979; Moore and Rymer, 2007); dynamic weakening processes including thermal pressurisation (Lachenbruch, 1980; Wibberley and Shimamoto, 2005) and coseismic shear heating (Hirose and Bystricky, 2007); and high pore fluid pressures (Rice, 1992).

Previous explanations for slip specifically on LANFs include combinations of elevated pore fluid pressure with low tensile strength (Axen, 1992; Collettini and Barchi, 2002), weakening of fault rocks through reaction softening (Taylor and Huchon, 2002), and stress rotations either in the fault core (Axen, 1992) or at the base of the seismogenic zone (Westaway, 1999, 2005). The nucleation of LANFs within intact rock is also problematic. Stress rotations in sedimentary layers with contrasting viscosities have been invoked to account for listric normal fault geometries, where the fault dip decreases downwards (Bradshaw and Zoback, 1988), but only the relative viscosities were quantified.

The recurrence interval for large earthquakes on LANFs may be large, but this does not mean the seismic hazard is low (Wernicke, 1995). It is important to fully understand the mechanics of LANFs in order to reliably quantify the risks and to define potential earthquake precursors.

1.2. Rationale

Changes in material properties lead to changes in the local stress field (Casey, 1980). This concept of stress rotation has been applied to strike–slip faults (Rice, 1992; Faulkner et al., 2006; Healy, 2008) and LANFs (Axen, 1992; and this paper). Bradshaw and Zoback (1988) used contrasting viscosities of sandstone and shale in sedimentary sequences to generate stress rotations and explain listric normal faults in the Gulf of Mexico. Note that both the viscous

* Tel.: +61 (0)8 9266 7969; fax: +61 (0)8 9266 3153.
E-mail address: d.healy@curtin.edu.au

0191-8141/$ – see front matter © 2009 Elsevier Ltd. All rights reserved.
doi:10.1016/j.jsg.2009.03.001

(Bradshaw and Zoback, 1988) and von Mises plastic (Rice, 1992) approaches contain a fundamental limit in the amount of stress rotation possible; the most compressive principal stress (σ_1) can only rotate to 45° of the fault zone boundary. This may not be sufficient to promote fault-parallel slip.

Natural fault zones are characterised by one or more narrow core zones flanked by wider damage zones (Flinn, 1977). Foliated fault core rocks possess intrinsic anisotropy from the strong preferred alignment of phyllosilicate minerals (Chester et al., 1985; Rutter et al., 1986) and extrinsic anisotropy from arrays of grain boundary pores and microcracks. Due to the aspect ratios and shape preferred orientations of platy phyllosilicates in these rocks, most of these grain boundary microcracks are parallel to the mineral foliation. There are however very few laboratory measurements of fault core rock elastic properties, with the exception of some mylonites and phyllonites (Jones and Nur, 1982; Kern and Wenk, 1990), and these measurements were made under dry loading, such that all microcracks and pores were closed.

In this paper, the material properties of foliated, anisotropic fault core rocks are quantified with crack damage models based on Effective Medium Theory (EMT; Kachanov, 1993). EMT has a robust theoretical basis in solid mechanics and has been validated by numerous rock deformation experiments (see Section 2.1). The elastic anisotropy of fault core rocks can be predicted using intrinsically anisotropic proxies (e.g. shale, serpentinite, schist) and adding extrinsic anisotropic damage (Fig. 1) in the form of crack arrays. These cracks define a porosity and allow us to explore fluid saturated conditions using poroelasticity (see Section 2.2).

It has recently been shown that significant rotations of σ_1 towards the fault zone are only predicted when the crack damage is oriented parallel to the fault zone, and this is most likely in the fault core (Healy, 2008). The classical behaviour of isotropic porous materials with changes in pore fluid pressure is well known, and involves no changes in effective shear stress (e.g. Jaeger et al., 2007). However, Chen and Nur (1992) showed how two different patterns of extrinsic anisotropy (e.g. crack damage) can combine with variations in pore fluid pressure to generate counterintuitive changes in effective normal stress *and* shear stress (Section 3).

The aims of this paper are to explore how anisotropic poroelastic rocks behave in terms of pore fluid pressure changes, and then to apply these findings to a generic model of LANF nucleation and evolution (Sections 4–6). The focus here is on a simplified static poroelastic response, while accepting that time-dependent (viscous) and chemical processes are important in natural examples. In this paper, the general term 'cracks' is used for tectonically induced brittle microcracks, inequant grain boundary cracks and pores.

2. Anisotropy, Effective Medium Theory and poroelasticity

2.1. Effective Medium Theory

Rock deformation experiments indicate that changes in the proportion of cracks alter the bulk elastic properties of a rock (Brace et al., 1966). While increases in confining pressure lead to small increases in elastic stiffness, increasing deviatoric stress towards the yield strength generates marked decreases in elastic stiffness (Scott et al., 1993; Sayers and Kachanov, 1995). Conceptually, these effects can be understood in terms of the opening and closing of cracks along the loading path. A more rigorous and quantitative foundation is provided by the Effective Medium Theory (EMT) of Kachanov (1993).

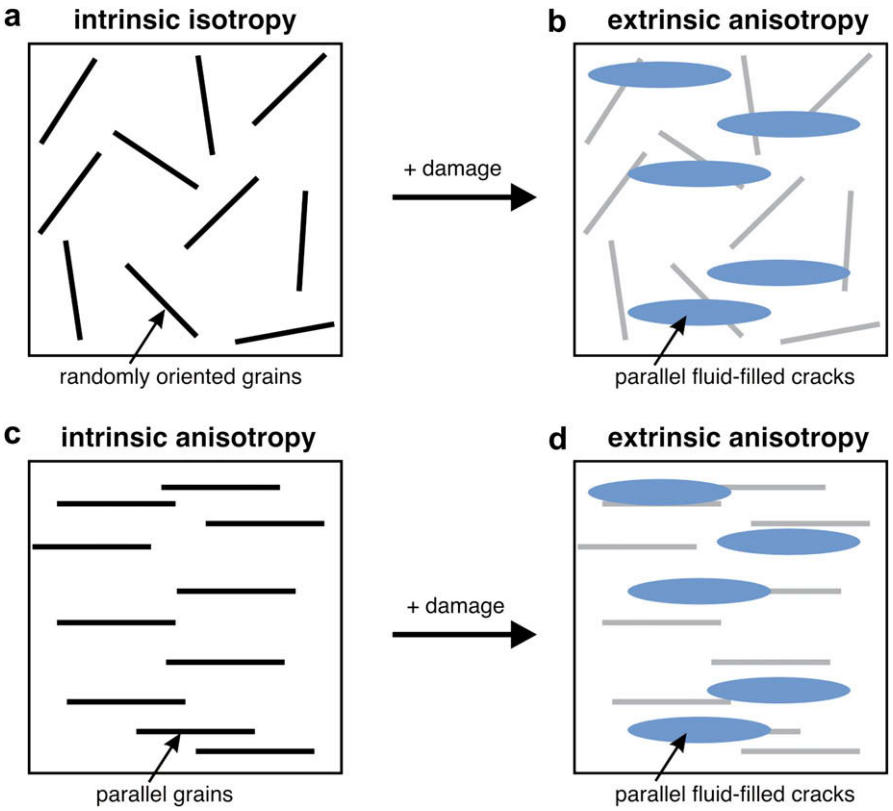

Fig. 1. Schematic diagrams to distinguish between intrinsic and extrinsic components of anisotropy. (a and b) Randomly oriented mineral grains in an intact rock constitute intrinsic anisotropy; extrinsic anisotropy is then added in the form of parallel crack damage. (c and d) Foliated rocks with aligned grains possess intrinsic anisotropy; the addition of crack damage (extrinsic anisotropy) reinforces the original anisotropy.

EMT links crack density to elastic compliance. The crack density is defined as a tensor, which captures the effects of any orientation distribution in the cracks. The second order crack density tensor $\boldsymbol{\alpha}$ is defined as:

$$\boldsymbol{\alpha} = (1/V)\sum_{N} a^3 \mathbf{nn} \tag{1}$$

where V is the volume, N is the number of cracks in this volume and a is the radius of a penny-shaped flat crack, with unit normal $\mathbf{n}$. A scalar crack density, ignoring any orientation distribution of the cracks, can be expressed as:

$$\rho = tr\boldsymbol{\alpha} = (1/V)Na^3 \tag{2}$$

An additional fourth order crack density tensor has no significant effect on the compliances for 'dry' cracks (Sayers and Kachanov, 1995), and only 'dry' crack damage is used in this paper (see Section 2.2).

The effective compliance S_e of a cracked rock is written as:

$$S_e = S_i + \Delta s \tag{3}$$

where S_i is the original compliance of the intact rock and Δs describes the effects of the cracks:

$$\Delta s_{ijkl} = \left[8(1-\nu^2)/3E(2-\nu)\right]\left(\boldsymbol{\alpha}_{ik}\boldsymbol{\delta}_{jl} + \boldsymbol{\alpha}_{il}\boldsymbol{\delta}_{jk} + \boldsymbol{\alpha}_{jk}\boldsymbol{\delta}_{il} + \boldsymbol{\alpha}_{jl}\boldsymbol{\delta}_{ik}\right) \tag{4}$$

where $\boldsymbol{\delta}$ is the Kronecker delta, and E and ν are Young's modulus and Poisson's ratio of the intact rock, respectively. The changes in elastic compliance are therefore a direct function of the number of cracks (N) and their orientation distribution ($\mathbf{n}$). An initially isotropic rock will in general be degraded to a lower elastic symmetry due to increasing crack damage, with compliance values increasing with crack density. Explicit expressions for all elements of Δs can be found in Guéguen and Sarout (2009).

Results from rock deformation experiments support the use of EMT to describe damage evolution and the changes to elastic properties. Schubnel et al. (2003, 2006) inverted measurements of elastic wave velocities during the deformation of granite, basalt and marble, with a good correspondence between EMT predictions and experimental observations. Katz and Reches (2004) also validated the EMT approach by mapping microcrack damage in experimentally deformed granite samples. The detail of these laboratory studies has yet to be matched by field studies, although Rabbel et al. (2004) inverted seismic velocity measurements in the KTB deep borehole to calculate elastic stiffnesses near a major fault zone. The KTB data show a progressive decrease in 5 elastic stiffness coefficients (i.e. increases in compliance) as the fault is approached at a depth of ~8 km.

In summary, the EMT approach of Kachanov (1993) provides a theoretical basis for the evolution of damage in rock and the related changes in elastic properties. Moreover, the quantitative comparison of data from samples of both crystalline and sedimentary rocks deformed under controlled laboratory conditions (e.g. Schubnel et al., 2006; Sarout and Guéguen, 2008) confirms that the theory accurately predicts the effects of crack damage in a tractable form.

2.2. Anisotropic poroelasticity

The anisotropy discussed in this paper is simplified to the case of a single array of parallel cracks. Changed elastic compliances are calculated for a prescribed value of scalar crack density and added to the intact compliance using Equation (3). The elastic stiffness is easily obtained by inverting the compliance tensor (e.g. Nye, 1985). The elastic compliances are calculated using the 'dry' crack formulation of EMT, which is the correct approximation for the static response of a saturated fault zone to long-term loads. Recall that the elastic response of saturated rocks is frequency dependent (Guéguen and Sarout, 2009). For high frequency or ultrasonic (~MHz) measurements on laboratory scale samples, the unrelaxed formulation of EMT accurately captures the elastic response. Subjected to loads at high frequencies, the fluid in the rock is stationary within the cracks and pores, and pore fluid pressure varies over the Representative Volume Element (RVE) (Fig. 2a). However, for static (0 frequency) or low frequency loads (~Hz) the relaxed formulation of EMT applies, the fluid is able to move in the cracks and pores over the time scale of the loading, and pore fluid pressure is constant (isobaric) in the RVE (Fig. 2b). For this static, relaxed state we can couple EMT with poroelasticity to explore the combined effects of changes in elastic properties (i.e. crack damage) with changes in pore fluid pressure, and see how they influence the mechanical response of a fault zone.

To investigate the combined effects of fluids and anisotropy in fault zones, the effective stresses are calculated according to the following equation (Chen and Nur, 1992):

$$\sigma'_{ij} = \sigma_{ij} - P_f \boldsymbol{\beta}_{ij} \tag{5}$$

where σ' is the effective stress tensor, P_f is pore fluid pressure and the Biot tensor $\boldsymbol{\beta}$ is calculated from (Carroll, 1979):

$$\boldsymbol{\beta}_{ij} = \boldsymbol{\delta}_{ij} - c_{ijkl}s^{i}_{klmm} \tag{6}$$

where c_{ijkl} is the stiffness of the damaged rock, s^{i}_{klmm} is the compliance of the intact rock and $\boldsymbol{\delta}$ is the Kronecker delta. The effective stress depends on the anisotropy through the Biot tensor. In this formulation (Equation (6)), there is no explicit term for porosity. The effects of the pore space, whether true pores or damage-induced cracks, are included in the stiffness tensor of the damaged rock (c_{ijkl}), calculated from EMT. For the anisotropic, foliated fault core rocks in this study, the porosity will be foliation-parallel grain boundary cracks and pores and therefore accurately captured by a stiffness tensor calculated with a parallel array of cracks. In the case of isotropy, the Biot tensor becomes the 2nd order identity tensor:

$$\boldsymbol{\beta}_{ij} = \boldsymbol{\delta}_{ij} \tag{7}$$

and the only effect of the pore fluid pressure is on the normal stress components.

3. Effective stresses in anisotropic rocks

3.1. Increased pore fluid pressure

For saturated isotropic rocks, only the normal components of the stress tensor are modified by the pore fluid pressure. With an increase in P_f, effective normal stresses are all reduced equally by an amount P_f, and there are no changes in shear stress (τ) or the differential stress (σ_d). For saturated anisotropic rocks, the inequant geometry and orientation distribution of the cracks and pores influence the effective stresses (Carroll, 1979; Chen and Nur, 1992). Extrinsic anisotropy (Fig. 1) in the form of non-random alignments of cracks and pores leads to changes in both the normal *and* the shear stresses. This has counterintuitive and important consequences for brittle failure (both shear and tensile) and frictional sliding. For example, in the classical isotropic case, increases of P_f tend to move the stress state towards failure and decreases in P_f promote stability. In the case of anisotropy, depending on the

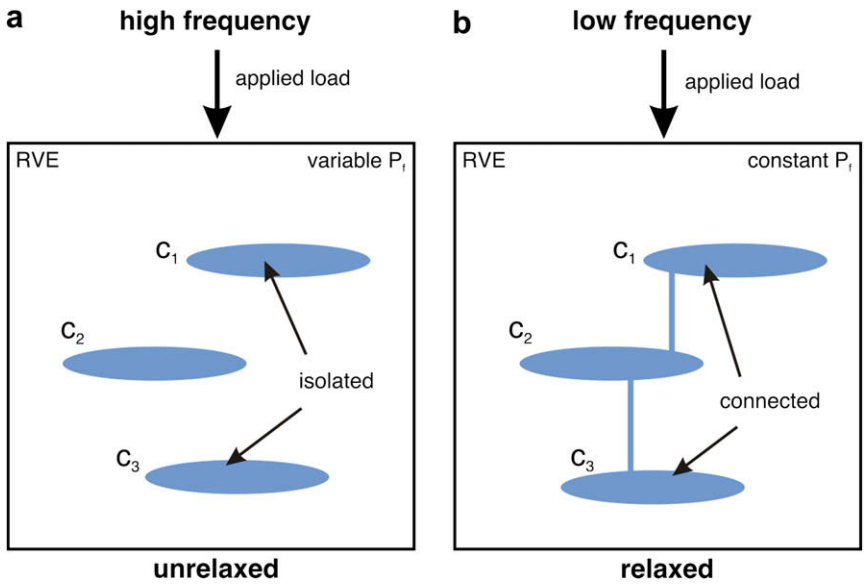

Fig. 2. Schematic diagrams to illustrate the difference between the unrelaxed (high frequency) and relaxed (low frequency) states of Effective Medium Theory. (a) In the unrelaxed case under high frequency loads (ultrasonic, MHz), the cracks and pores behave as though isolated and unconnected. The pore fluid cannot move quickly enough in response to the load, and P_f varies (non-isobaric) over the Representative Volume Element (RVE). (b) In the relaxed case under low frequency (Hz) or static (0 Hz) loads, the cracks and pores behave as a connected network. The pore fluid can move in response to the applied load, and P_f is constant (isobaric) over the RVE. The relaxed case is the domain of poroelasticity, and can be applied to static models of fault zones.

strength and orientation of the anisotropic fabric with respect to the applied stresses, the opposite effects are possible i.e. increasing P_f can promote stability. In detail, these effects are governed by the components of the Biot tensor ($\boldsymbol{\beta}$), itself a function of the intact compliance and the damaged stiffness (Equation (6)).

Examples serve to illustrate the interplay of the orientation of the anisotropy and changes in pore fluid pressure on the stress state in saturated anisotropic rocks. Mohr diagrams are shown in Fig. 3 for the stress state calculated for Berea sandstone, which is isotropic when intact (Table 1), and has a porosity of 15–20%. For the intact case, under a triaxially compressive load (see Fig. 3a), an increase in pore fluid pressure of 20 MPa leads to changes only in the normal stresses (Fig. 3b). Adding crack damage in the form of parallel cracks oriented perpendicular to σ_3 (Fig. 3c) and with a crack density of 0.4, changes the elastic properties compared to the intact state, and therefore the stress state changes (Fig. 3d). An increase in pore fluid pressure (+20 MPa) leads to changes in the Biot tensor and in turn this produces changes in the effective shear and differential stresses (Fig. 3d). For this orientation of anisotropy, defined by parallel cracks normal to σ_3, the overall effect of the increased P_f is the same as for the isotropic case: the stress state moves closer to the envelopes for frictional sliding and shear failure (Fig. 3d). If the anisotropy is instead defined by cracks or inequant pores oriented normal to σ_1 (Fig. 3e), the effect of a rise in P_f is reversed. The final stress state for the anisotropic rock is now further away from the frictional sliding and shear failure envelopes (Fig. 3f). This saturated anisotropic rock has experienced a rise in P_f, and yet becomes more stable, not less.

Table 1
Intact stiffness tensors, in Voigt notation (see Nye, 1985). All rocks, except the isotropic Berea sandstone, have transverse isotropy (i.e. hexagonal symmetry). Stiffness values are reported in GPa.

	c_{ij}	c_{i1}	c_{i2}	c_{i3}	c_{i4}	c_{i5}	c_{i6}
Sandstone	c_{1j}	38.83	4.80	4.80	0.00	0.00	0.00
Scott et al., 1993	c_{2j}	4.80	38.83	4.80	0.00	0.00	0.00
Berea	c_{3j}	4.80	4.80	38.83	0.00	0.00	0.00
$P_c = 0$	c_{4j}	0.00	0.00	0.00	17.02	0.00	0.00
	c_{5j}	0.00	0.00	0.00	0.00	17.02	0.00
	c_{6j}	0.00	0.00	0.00	0.00	0.00	17.02
Shale	c_{1j}	58.81	11.73	15.69	0.00	0.00	0.00
Vernik and Liu, 1997	c_{2j}	11.73	58.81	15.69	0.00	0.00	0.00
Bazhenov, 3812 m	c_{3j}	15.69	15.69	27.23	0.00	0.00	0.00
$P_c = 70$ MPa	c_{4j}	0.00	0.00	0.00	13.23	0.00	0.00
	c_{5j}	0.00	0.00	0.00	0.00	13.23	0.00
	c_{6j}	0.00	0.00	0.00	0.00	0.00	23.54
Serpentinite	c_{1j}	100.00	36.00	42.00	0.00	0.00	0.00
Song et al., 2004	c_{2j}	36.00	100.00	42.00	0.00	0.00	0.00
Average of 3	c_{3j}	42.00	42.00	85.00	0.00	0.00	0.00
$P_c = 70$ MPa	c_{4j}	0.00	0.00	0.00	24.00	0.00	0.00
	c_{5j}	0.00	0.00	0.00	0.00	24.00	0.00
	c_{6j}	0.00	0.00	0.00	0.00	0.00	34.00
Schist	c_{1j}	94.38	18.21	26.30	0.00	0.00	0.00
Godfrey et al., 2000	c_{2j}	18.21	94.38	26.30	0.00	0.00	0.00
Coldfoot, TA-80	c_{3j}	26.30	26.30	68.49	0.00	0.00	0.00
$P_c = 100$ MPa	c_{4j}	0.00	0.00	0.00	24.44	0.00	0.00
	c_{5j}	0.00	0.00	0.00	0.00	24.44	0.00
	c_{6j}	0.00	0.00	0.00	0.00	0.00	38.09

3.2. Decreased pore fluid pressure

Fig. 4 shows the same suite of models as in Fig. 3, but now with a decrease in P_f. Again, the isotropic case for the intact sandstone is well known, with shear stress and differential stress unchanged: the Mohr circle for the final stress state moves to the right by an amount $+P_f$ (Fig. 4b). For the anisotropic case of cracks oriented normal to σ_3, the decrease in P_f also stabilises the rock mass, as the Mohr circle shrinks away from the frictional sliding and shear failure envelopes (Fig. 4d). However, the anisotropic case of cracks or pores oriented normal to σ_1 produces an apparently anomalous result for a decrease in P_f, with the stress state moving closer to the frictional sliding and shear failure envelopes.

3.3. Effect of anisotropy orientation on effective stresses

It is clear from Figs. 3 and 4 that the orientation of the anisotropy with respect to the applied load exerts a significant influence on the

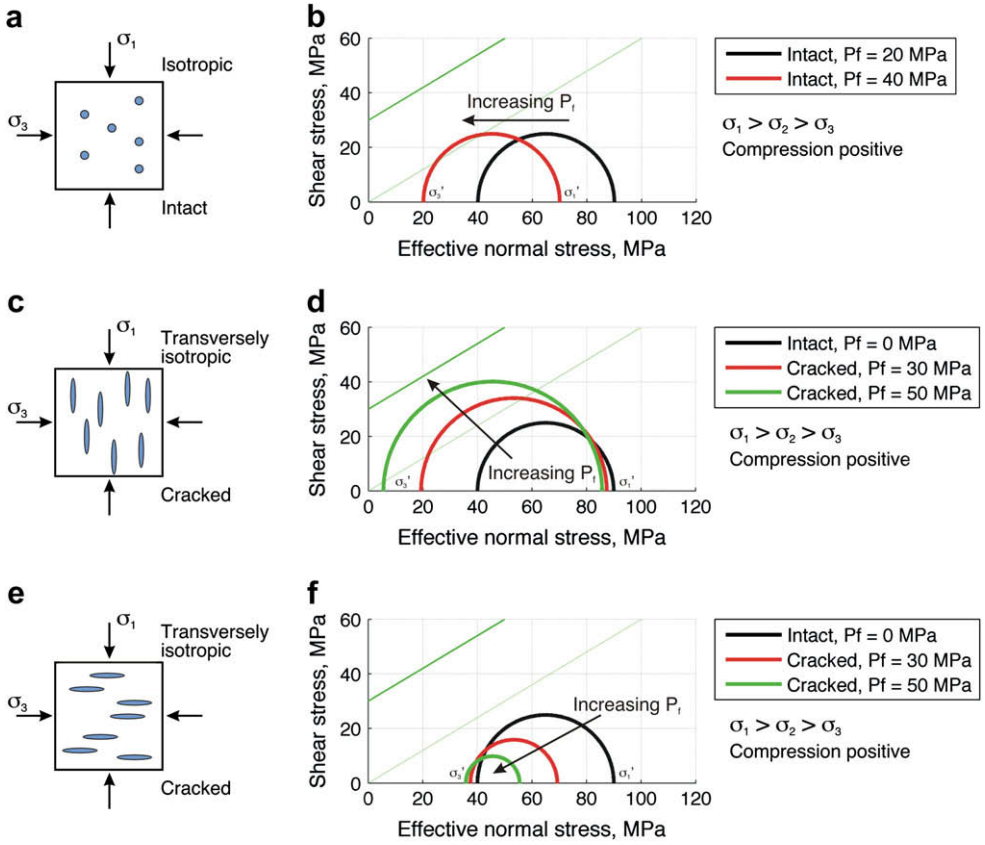

Fig. 3. Mohr diagrams showing the effects of increasing pore fluid pressure (P_f) in isotropic and anisotropic porous rocks. These examples use intact stiffness data for Berea sandstone (see Table 1). Straight lines show schematic failure criteria for shear fracture (solid line) and frictional sliding (dotted line). (a–b) For the intact rock, the porosity and matrix are isotropic. Increasing the pore fluid pressure (P_f) by 20 MPa, decreases the effective normal stresses but leaves the shear stress and differential stress unchanged. c–d) The addition of cracks with scalar crack density of 0.4 aligned normal to σ_3, and with $P_f = 30$ MPa shifts the intact stress state to a state of increased shear stress and possible frictional sliding. A further increase in P_f of 20 MPa in the cracked sandstone, enhances this effect and moves the rock towards shear failure. (d–e) For the case of cracks aligned normal to σ_1, and the same changes in P_f, the stress state moves away from frictional sliding; increased P_f makes this rock more stable, not less.

response of the rock mass to changes in pore fluid pressure. For simple anisotropies defined by parallel arrays of cracks added to intact Berea sandstone, the systematic variation of effective stress magnitudes with orientation is shown in Fig. 5. At low crack density ($\rho = 0.1$, Fig. 5a) and $P_f = 50$ MPa, the effective differential stress decreases as the cracks rotate from parallel to σ_1 to normal to σ_1. This effect is magnified for a higher crack density ($\rho = 0.5$, Fig. 5b).

These graphs show that for saturated anisotropic rocks with cracks and pores oriented at high angle to the maximum compression (σ_1), significant reductions in differential stress are coupled with increases in P_f. For this orientation of anisotropy with respect to σ_1, the reverse is also true; decreases in P_f can produce very large increases in differential stress.

3.4. Intrinsic anisotropy: shale, serpentinite and schist

The modelled changes in elastic properties shown so far, and in the cases shown by Chen and Nur (1992), have been based on parallel crack damage added to initially intact isotropic rocks. As noted in Introduction, there are no published laboratory measurements of elastic properties of rocks taken from the core zones of shallow crustal faults, and this partly reflects the technical difficulty in measuring elastic properties in weak, porous and foliated material. There are two further complications: decompression of natural samples during exhumation to the surface may significantly alter their microstructure prior to measurement in the laboratory; and the frequency dependence of elastic response for saturated rocks means that the elastic properties calculated from ultrasonic (high frequency, unrelaxed) measurements bear no simple relationship to the elastic properties in situ (low frequency, relaxed; see Guéguen and Sarout, 2009). EMT can be used to calculate plausible values of elastic properties for fault core rocks, by combining the effects of intrinsic anisotropy due to strong lattice and/or shape preferred orientations of phyllosilicates in the rock matrix and extrinsic anisotropy from grain boundary cracks and inequant pores. Note that Equation (3) is not limited to isotropy in the intact compliances: intrinsic anisotropies are also valid.

Laboratory measurements of selected highly anisotropic phyllosilicate-rich lithologies are shown in Table 1. These measurements were taken at confining pressures, ranging from 70 to 100 MPa, and under dry conditions such that existing pores and cracks were closed. These values are therefore believed to accurately record the intact, intrinsic elastic stiffness of the various rock types. Stress states in the intact rocks are shown in the Mohr diagrams in Fig. 6a–c. Extrinsic anisotropy has then been added with an array of cracks aligned parallel to the intrinsic (matrix) anisotropy, at a modest scalar crack density of 0.25. Using the calculated elastic stiffnesses in Equation (6) and with $P_f = 30$ MPa, the stress state is much reduced in all cases (Fig. 6a–c). A further increase in P_f of +20 MPa in these damaged rocks, leads to significant further reductions in differential stress (Fig. 6a–c).

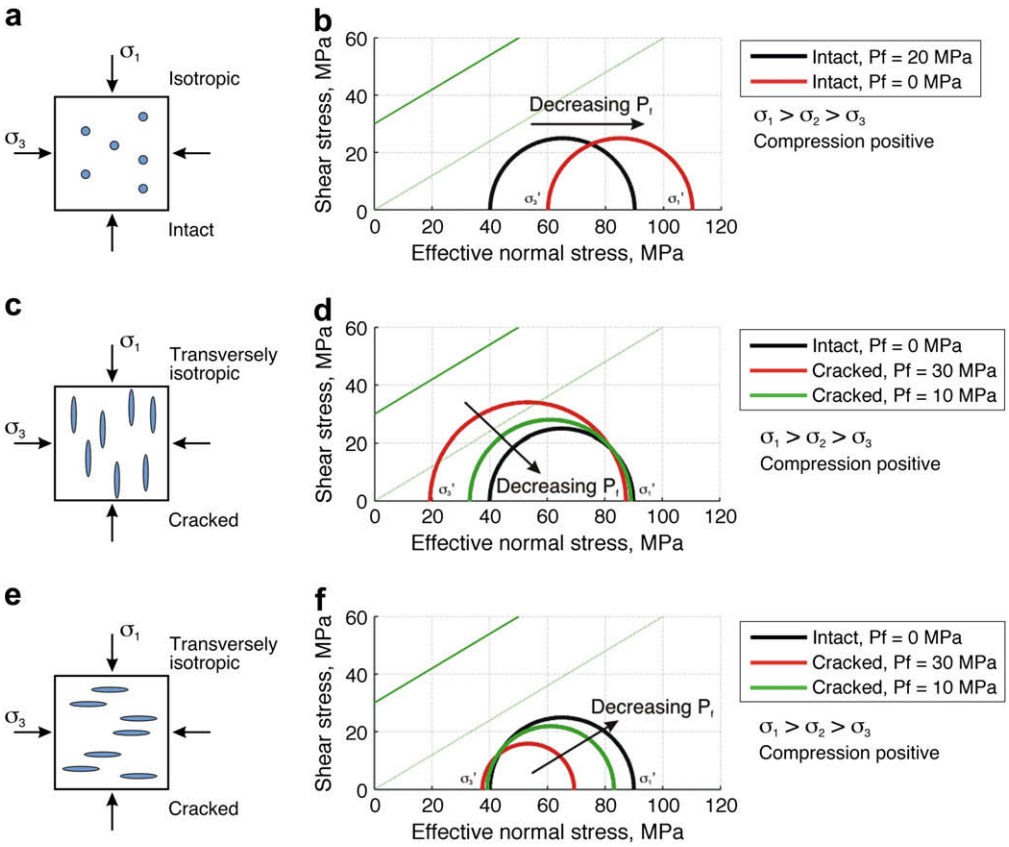

Fig. 4. Mohr diagrams showing the effects of decreasing P_f in isotropic and anisotropic cracked rocks, again using stiffness data for Berea sandstone (Table 1). (a–b) For the intact isotropic rock, decreasing the pore fluid pressure (P_f) by 20 MPa, increases the effective normal stresses but leaves the shear stress and differential stress unchanged. (c–d) The addition of cracks with scalar crack density of 0.4 aligned normal to σ_3, and with $P_f = 30$ MPa shifts the intact stress state to a state of increased shear stress and possible frictional sliding. A subsequent decrease in P_f of 20 MPa reverses this effect and moves the rock away shear failure and frictional sliding. (d–e) For the case of cracks aligned normal to σ_1, and the same changes in P_f, the cracked stress state moves closer to frictional sliding; decreased P_f makes this rock less stable, not more.

These phenomena have important implications for stress states in the core zones of LANFs, and 'weak' faults in general (Healy, 2008). Foliated and saturated rocks in the core zone of many LANFs possess significant elastic anisotropy. It is widely accepted that LANFs are misoriented with respect to a regionally subvertical, maximum compressive stress. For saturated, anisotropic rocks, the results from the preceding sections show that the orientation of the total (intrinsic + extrinsic) anisotropy with respect to the applied

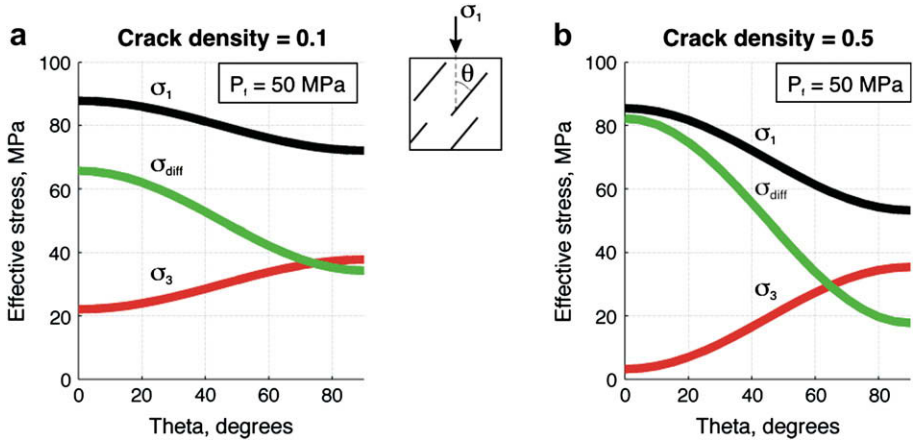

Fig. 5. Graphs showing the relationship between the orientation of anisotropy defined by parallel cracks and the stress state. Angle theta is measured between the plane of the cracks and σ_1 (see inset). Effective principal stresses σ_1 and σ_3 are shown together with effective differential stress, σ_d. (a) Berea sandstone with a low crack density ($\rho = 0.1$) shows decrease of effective differential stress, σ_d as the plane of isotropy, parallel to the cracks, rotates from 0° to 90° with σ_1. (b) For a higher crack density ($\rho = 0.5$) and the same load and pore fluid pressure, this drop in σ_d is vastly increased.

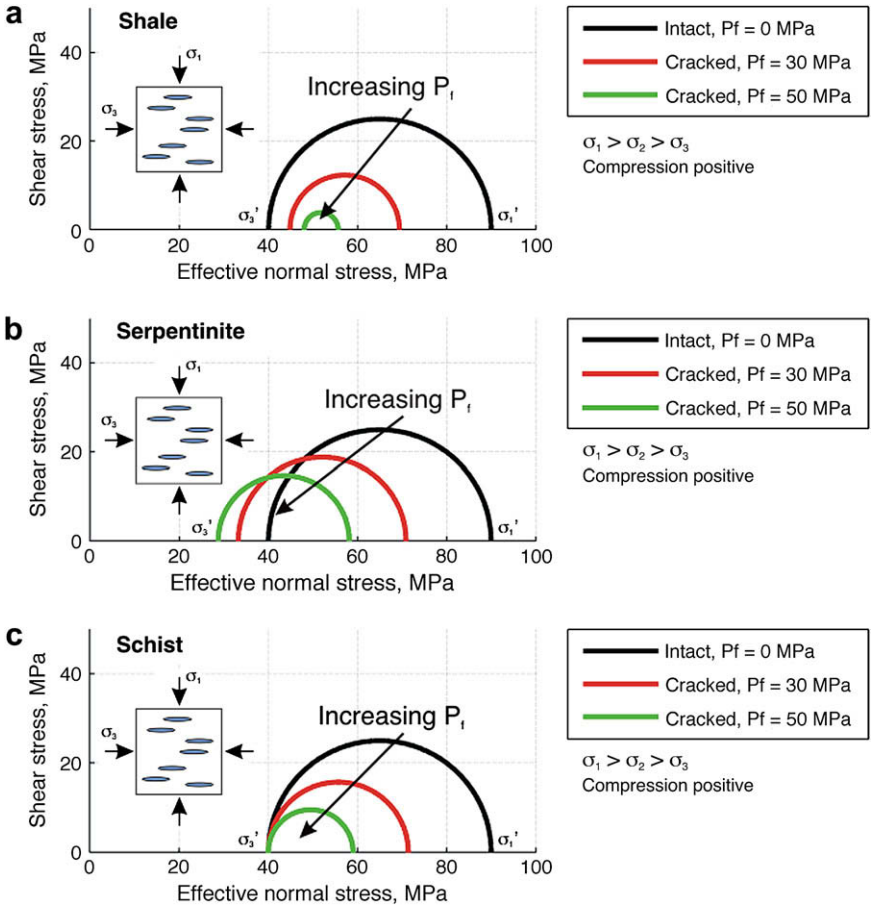

Fig. 6. Mohr diagrams for anisotropic rocks with increases in P_f. All three examples have the same initial stress state for the intact rock, and the damaged rocks have a constant crack density of 0.25 with $P_f = 30$ MPa. A constant increase in P_f of +20 MPa is shown for each case. The intact elastic stiffnesses have been taken from laboratory measurements made at elevated P_c (see Table 1). (a) Shale. (b) Serpentinite. (c) Schist. In all cases (a–c), the reduction in σ_d for the damaged rock means that further increases in P_f will most likely lead to tensile failure and not shear failure, and that these increases in P_f will need to be very large.

load is critical in determining the response to variations in P_f. Importantly, this response can be counterintuitive when compared to the common simplifying assumption of isotropy.

4. LANFs and their association with HANFs, veins and fluids

4.1. Woodlark detachment fault, SW Pacific

The Woodlark detachment is located in continental crust at the western end of a propagating oceanic ridge system (Abers, 1991). The fault dips at a low angle ($\sim 25^\circ$) towards the north (Floyd et al., 2001) and is seismically active (Abers, 1991; Abers et al., 1997). Results from ODP leg 180 have provided a wealth of data on the fault core zone, the footwall and hanging wall, and the regional setting (see Table 2; Taylor and Huchon, 2002). The fault core zone is between 30 and 60 m thick and comprises foliated talc–chlorite–serpentinite gouge, foliated cataclasites and mylonites (Floyd et al., 2001; Roller et al., 2001). The fault zone displays permeability anisotropy, with along-fault permeability about twice the across-fault value (Kopf, 2001). Brecciated and veined damage zones extend into the metagabbros of the footwall and the turbiditic sandstones of the hanging wall. There is overwhelming evidence for high pore fluid pressures around the fault core zone, including low seismic *P*-wave velocities along the highly reflective core zone (Floyd et al., 2001), multiple generations of carbonate-dominated tensile veins from drill-core samples (Kopf et al., 2003) and a present day flux of CO_2-rich hydrothermal fluids from a source deeper than 7 km (Famin and Nakashima, 2005). Tensile veins are oriented parallel and at high angles to the fault core fabric (Roller et al., 2001; Kopf et al., 2003). Seismic reflection surveys show large (several kilometres down-dip length) high-angle normal faults (HANFs) in the hanging wall and in the footwall, and these faults are also seismically active (Abers et al., 1997).

4.2. Zuccale fault, Elba

The Zuccale fault is located on the island of Elba, off the western coast of Italy (Keller and Pialli, 1990). The fault is now inactive and has been deformed by later movements, but originally dipped at a low angle ($<15^\circ$) to the east (Collettini and Holdsworth, 2004). The fault core zone contains a complex assemblage of foliated rocks and is between 10 and 20 m thick (Table 2). Multiple generations of tensile veins cut the fault core zone, with earlier veins rotated towards the fault-parallel fabric (Collettini et al., 2006). Further evidence for high pore fluid pressures comes from fluidised fault breccias, which exploit footwall faults to intrude and cut the fault core fabric (Smith et al., 2008a). The vein mineralogy and the fluidised breccia cements are dominated by carbonates, which correlate with a high regional flux of CO_2, much of it with a mantle signature (Chiodini et al., 2000). Stable isotope data from the veins suggest an igneous source for the vein fluids during the early history of the fault, evolving to shallower mixed sources during

Table 2
Key features of the Woodlark detachment fault and the Zuccale fault.

Woodlark detachment fault, SW Pacific	
Seismically active, including M_W 6.8 in 1985	Abers, 1991; Abers et al., 1997
High pore fluid pressure inferred from reflective seismic low velocity zone and hydrothermal veins	Floyd et al., 2001
Fault core dips ~25°, ~30–60 m thick	Floyd et al., 2001; Kopf et al., 2003
Evidence for CO_2-rich hydrothermal fluids, sourced deeper than 5–7 km	Famin and Nakashima, 2005
High-angle normal faults in FW and HW	Taylor and Huchon, 2002
Foliated fault core rocks including talc–chlorite–serpentinite, cataclasite and mylonite	Kopf et al., 2003; Famin and Nakashima, 2005
Veining dominated by carbonate; multiple generations of tensile veins	Kopf et al., 2003; Famin and Nakashima, 2005
Higher permeability measured along fault rock fabric than across	Kopf, 2001
Zuccale fault, Elba	
Seismically inactive	Collettini and Barchi, 2002
High pore fluid pressures inferred from fluidised breccias and hydrothermal veins	Smith et al., 2008a
Fault core dips <15°, ~10–20 m thick	Collettini and Holdsworth, 2004
Regional CO_2 flux, much of it with a mantle signature	Chiodini et al., 2000
High-angle normal faults in FW and HW	Smith et al., 2007
Foliated fault core rocks including talc schist, cataclasite and phyllonite	Collettini and Holdsworth, 2004
Veins dominated by carbonate; multiple generations including some sheared into concordance with fault rock fabric	Collettini et al., 2006

later exhumation (Smith et al., 2008b). The footwall and hanging wall both contain HANFs. The footwall HANFs have displacements up to several metres, and are tens of metres in down-dip length. These footwall structures may have deactivated before the final movements on the LANF (Smith et al., 2007), whereas some of the hanging wall faults appear to sole into the shallow dipping LANF (Collettini and Holdsworth, 2004).

4.3. Generalisations

These two well documented examples illustrate a pattern (Table 2) common to other cases: LANFs do not exist in spatial or temporal isolation, but form part of a complex system with LANFs and HANFs both contributing to regional extension e.g. Basin and Range, western USA (Davis et al., 1980; Hayman et al., 2003), Apennines, central Italy (Collettini and Barchi, 2002) and Corinth, Greece (Rietbrock et al., 1996). This coupling between LANFs and HANFs is also apparent over much shorter time scales of triggered seismicity (Axen, 1999). LANFs often record evidence for high pore fluid pressures and/or tensile veining in and around the fault core zone. LANFs, in common with other 'weak' faults, often display core zones with foliated, anisotropic fault rocks. The combination of fluid saturation and elastic anisotropy in the LANF fault core and the presence of HANFs in the footwalls and hanging walls need to be accounted for in any generic model.

5. Formation of LANFs

5.1. Stress rotations in anisotropic layered sequences

The stress rotation model for the formation of listric normal faults based on viscosity contrasts (Bradshaw and Zoback, 1988) is readily extended to the initiation of LANFs in sedimentary basins. Many sedimentary rocks exhibit intrinsic elastic anisotropy to some degree (e.g. Valcke et al., 2006), but shales are often much more anisotropic due mainly to the shape and lattice preferred orientations of clay minerals (e.g. Vernik and Liu, 1997; Dewhurst and Siggins, 2006). Pore fluid overpressures encouraged by low values of permeability across shale laminations and the generation of hydrocarbons in kerogen-rich shales (Vernik, 1994) can generate additional extrinsic anisotropy in the form of extensive bedding parallel cracks and inequant pores. A dipping shale layer enclosed in relatively isotropic sandstones with lithostatic, vertical maximum compressive stress will promote stress rotations away from the vertical on account of the contrast in elastic properties (Fig. 7a, and see Casey, 1980). Using intact elastic stiffnesses of sandstone and shale (Table 1), a simple 3 layer model with beds dipping at 10° leads to rotation of σ_1 to within 30° of the shale bedding (Fig. 7a). Simple Coulomb failure theory then predicts shear failure surfaces parallel to bedding. Small amounts of extrinsic crack damage aligned parallel to an intact shale fabric combined with increases in P_f promote further rotations of σ_1 towards bedding (Fig. 7b). Sliding parallel to the original compaction fabric in the shale will promote shear fabric development and a higher degree of elastic anisotropy (Dewhurst et al., 1996), which effectively acts as a positive feedback mechanism.

5.2. Stress rotations in isotropic weak zones

Serpentinisation of mafic and ultramafic igneous rocks at and below the sea floor leads to massive changes in material properties. Much of this alteration occurs in conditions of hydrostatic stress, or very low deviatoric stresses, and the textures of the serpentinites are often close to random (Andreani et al., 2007). Elastic anisotropy is not a prerequisite for the stress rotation model of Casey (1980), and isotropic changes in elastic stiffness can lead to significant rotations of σ_1. In the isotropic case, the critical component of the elastic stiffness is Poisson's ratio of the 'weak' layer (Healy, 2008). Laboratory measurements have shown that an increasing degree of serpentinisation is correlated with an increase in Poisson's ratio (ν) to values > 0.3 (Watanabe et al., 2007). Fig. 7c shows a simple 3 layer model of a shallow dipping isotropic serpentinite layer enclosed by gabbro. Rotation of σ_1 in the altered layer is controlled by ν, and for values of $\nu > 0.3$ significant stress rotations are feasible (Fig. 7d). Rock deformation experiments have shown that cataclasis under dry conditions also leads to increases in Poisson's ratio (Ayling et al., 1995; Fortin et al., 2007). Localised layers of granular, cataclastic gouge could therefore promote stress rotations. Cataclastic compaction bands, which form normal to σ_1, could generate significant stress rotations if the bands were subsequently rotated.

6. Evolution of LANFs

6.1. LANFs in the context of elevated pore fluid pressure

LANFs are associated in time and space with HANFs and elevated pore fluid pressures. A generic model for LANF formation and evolution needs to incorporate these key observations. In this section, the evolution of a rock mass containing an LANF core and flanking footwall and hanging wall is described in three temporal stages based on the spatial location of elevated fluid pressure. The fluid flux from dehydration and decarbonation reactions in deeper levels of the crust and mantle and from hydrothermal systems above igneous intrusions may be quasi-continuous or pulsed. However, for fluids migrating from depth, the fluid pressure will vary in a cyclic manner due mainly to the low value of across-fault permeability in the LANF core zone (Section 4). The three temporal stages described in this section are based on the location of an upwardly migrating fluid pressure pulse in the footwall (Stage 1), the fault core (Stage 2) and the hanging wall (Stage 3). While this

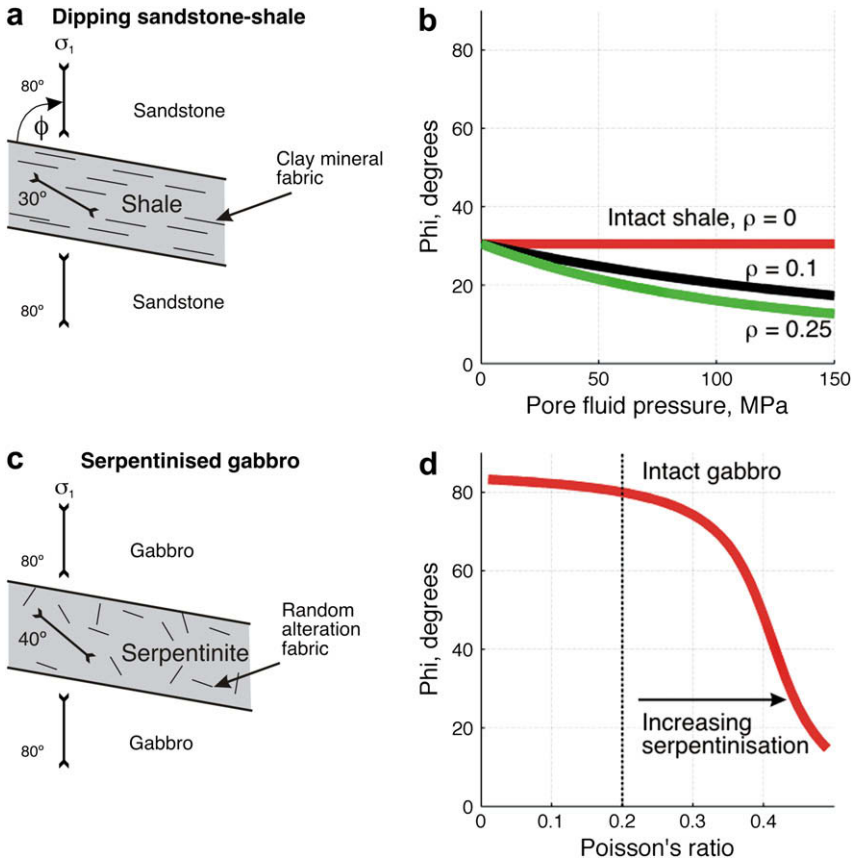

Fig. 7. LANF nucleation mechanisms based on stress rotations in layered sequences with heterogeneous elastic properties. (a and b) For a dipping sedimentary sequence of sandstone and shale, elastic anisotropy and lower elastic moduli in the shale promote rotation of σ_1 from vertical in the host sandstone to $\sim 30^\circ$ in the shale. Adding crack damage, even at low crack densities of 0.1–0.25, changes the elastic properties and promotes further rotation of σ_1 towards parallelism with the shale bedding. This crack damage needs not to be tectonic cracks *per se*, but inequant grain boundary porosity or cracking from hydrocarbon generation (e.g. Vernik, 1994). (c and d) Serpentinisation of a mafic protolith will change the elastic moduli and promote stress rotations. Increasing serpentinisation (at low T) is correlated with an increase in Poisson's ratio (Watanabe et al., 2007). Even if this alteration generates a random fabric, and the resulting elastic properties are isotropic, an increase in Poisson's ratio > 0.3 will promote large rotations of σ_1 towards parallelism with the boundaries of the altered layer.

temporal subdivision is arbitrary, it is useful to separate the effects of changing P_f on the wall rocks and the core to enable comparison with the data from the examples described in Section 4. These scenarios are only semi-quantitative – there is no explicit length scale, pore pressure magnitude or fluid flux rate, or any precise values for the effective stresses. Based on the theory described in Sections 2 and 3, the key factor governing the structural evolution is the interplay between the general direction of pore fluid pressure variation and the orientation of the anisotropy across the fault zone.

6.2. Stage 1 – fluid pulse in the footwall

At this stage of the cycle, the fluid pressure pulse is located in the footwall of the LANF. The fault core dips at a low angle (25° in Fig. 8a) and has a strong anisotropy oriented parallel to the edges. The extrinsic anisotropy from brittle microcracking in the footwall and hanging wall is vertical and normal to σ_3. Slightly rising P_f in the anisotropic fault core produces a decrease in σ_d (Fig. 8b), and the core is stable (no frictional sliding or shear failure), even for failure envelopes based on low coefficients of friction ($\mu \sim 0.2$–0.4) found in LANF fault cores (Numelin et al., 2007). Viscous creep by pressure solution in the core rocks at this stage will serve to strengthen the elastic anisotropy by intensifying the fabric. In contrast, the spike in P_f in the footwall combined with the vertical orientation of anisotropy destabilises the rock mass and HANFs are possible (Fig. 8c approaching shear failure envelope). The hanging wall is effectively protected from any significant changes in P_f by the low across-fault permeability of the core, and remains stable (Fig. 8d).

6.3. Stage 2 – fluid pulse in the fault core

As the high pressure fluid pulse moves into the fault core zone, the high degree of permeability anisotropy promotes along-fault flow (Fig. 9a; Kopf, 2001; Famin and Nakashima, 2005). An important result from Section 3.4 (Fig. 6) is that anisotropy in the fault core promotes a low differential effective stress, but note that tensile failure requires very high P_f (e.g. $\sim 10^2$ MPa). Multiple orientations of tensile veins in the Zuccale fault support the prediction of very low differential stresses, as required for the stress switching mechanism (Fig. 9b; Collettini et al., 2006). The sub-horizontal vein set at Zuccale and the fabric parallel veins in the Woodlark detachment core are oriented approximately normal to the regionally vertical σ_1. Opening of veins in this orientation implies temporary attainment of supralithostatic pore fluid pressures. These fault-parallel veins are directly analogous to the 'fault-veins' observed in high-angle reverse faults (also misoriented with respect to the regional stress), and record the LANF equivalent of 'fault valve' behaviour (Sibson, 1992). Decreasing P_f in the footwall

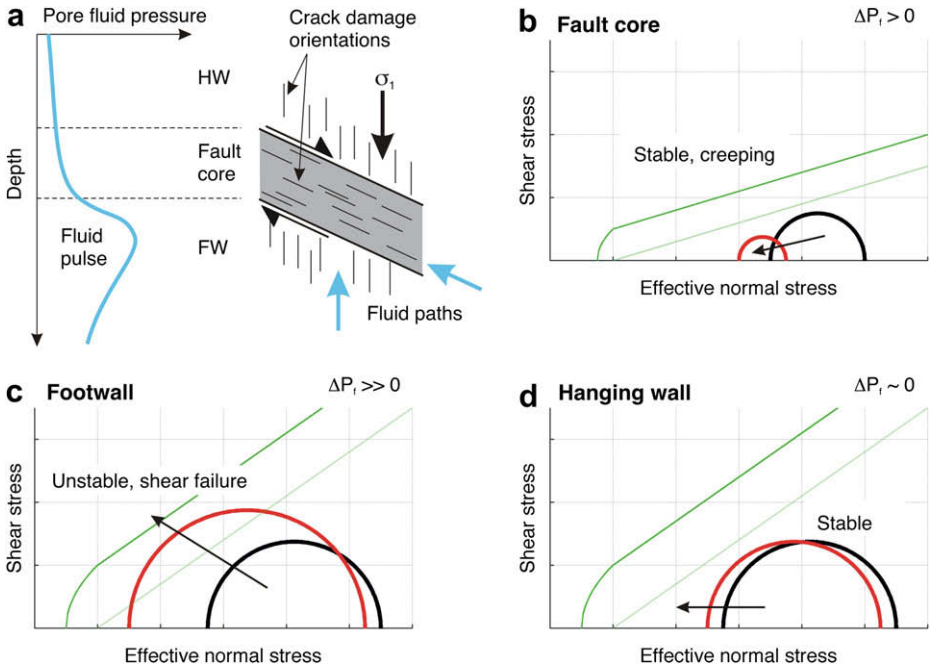

Fig. 8. Stress states in a low angle normal fault core, footwall and hanging wall. (a) At this stage the high pore fluid pressure (P_f) pulse is located in the footwall. Crack damage in the footwall and hanging wall is vertical, but parallel to the fault boundaries in the core. The orientations of these anisotropies control how changes in pore fluid pressure alter the effective stresses. (b) In the fault core, a slight increase in P_f in cracks aligned parallel to the fault zone causes the effective stresses to drop. The decrease in σ_d means the fault core is further from frictional sliding, i.e. more stable. (c) In the footwall (FW), with vertically oriented damage anisotropy, the large increase in P_f leads to a large increase in σ_d and shifts the stress state past frictional sliding and towards shear failure. Reactivation and nucleation of high angle normal faults are likely. (d) In the hanging wall (HW), the changes in P_f are very small due to the low vertical permeability of the fault core. A small increase in P_f will have negligible effect on the HW stress state.

serves to stabilise any HANFs in this region (Fig. 9c). The hanging wall is still protected from the fluid pressure pulse and only small changes in stress state are likely (Fig. 9d).

6.4. Stage 3 – fluid pulse in the hanging wall

As the fluid pressure pulse migrates into the hanging wall, the sudden and large decrease in fluid pressure in the fault core caused by earlier hydrofractures pushes the stress state back towards frictional sliding, with a marked increase in σ_d (Fig. 10b, compare with Fig. 4f). Seismic slip is now a possibility in the LANF core. The timing of this frictional slip in relation to the previous fluid loss is supported by the association of intrusive fluidised breccias in the Zuccale fault core with discrete slip patches of similar dimensions (Smith et al., 2008a). Sharp frictional sliding surfaces in the Zuccale fault core post-date local fluidised breccias, and these slip surfaces are concentrated immediately above the fluidised breccias. The longer term (interseismic) effect of these discrete brittle episodes is to promote further healing by pressure solution in the fault core rocks (Gratier et al., 1999), which in turn reduces across-fault permeability and promotes the next cycle of pore pressure build-up. The tensile veins in the fault core from the previous stage will be rotated towards concordance with the shear fabric (Fig. 10a) by this viscous creep. In the footwall, P_f will start to rise as the next fluid pulse migrates upwards, gradually moving the footwall rocks towards further frictional sliding on existing HANFs (Fig. 10c). The rise of P_f in the hanging wall pushes the stress state towards shear failure on new and pre-existing HANFs (Fig. 10d).

6.5. Synthesis

The sequence of events in response to an upwardly migrating fluid pressure pulse can be summarised as follows:

1. With the fluid pressure pulse in the footwall, HANFs are likely beneath the fault core. The fault core is stable (in terms of sliding or shear failure) and likely deforming by viscous creep mechanisms such as pressure solution. The hanging wall is also stable at this stage.
2. When the fluid pressure pulse reaches the LANF core, permeability anisotropy directs fluid flow along the fault and, if P_f rises high enough, tensile fracturing can occur. The footwall stabilises as P_f drops beneath the core zone. The hanging wall remains stable.
3. After the fluid pressure pulse reaches the hanging wall, seismic shear failure is now possible in the LANF core, with frictional sliding induced by the massive drop in P_f in these anisotropic rocks. The footwall HANFs may reactivate as P_f starts to build with the rise of the next fluid pulse.

The combined effect of the fault-parallel anisotropy and elevated pore fluid pressure in the fault core reduces differential effective stress in comparison to an isotropic equivalent, and therefore tends to stabilise the core. The effects of a sudden, large drop in P_f after any tensile failure in the core zone are exacerbated by the fault-parallel anisotropy, and can lead to seismic slip (i.e. frictional sliding) events.

The temporal evolution described above is based on a deep-seated fluid source moving up through the footwall (e.g. Smith et al., 2008a), but fluid transport could be restricted to the fault core and damage zones. Anastomosing and coalescing polymodal fault patterns observed in many fault zones provide highly connected pathways for fluid migration (Wibberley et al., 2008; Healy et al., 2006a,b). In this case, the effects of pore fluid pressure variations on the formation and reactivation of HANFs in the footwall and hanging wall would be much more localised (Reynolds and Lister, 1987; Axen and Selverstone, 1994). Several studies have suggested a role for meteoric or shallow fluid sources in the evolution of

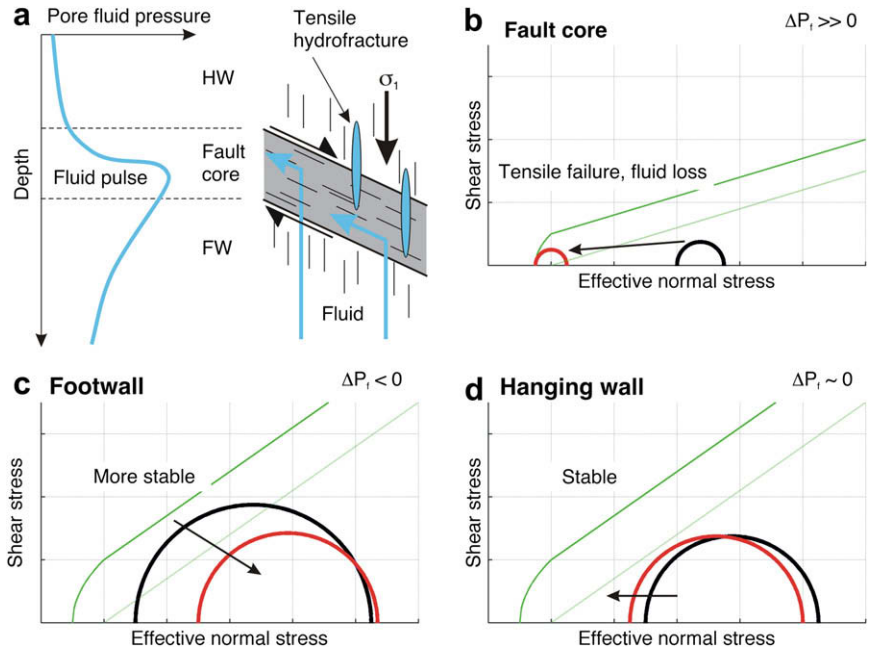

Fig. 9. Stress states in and around a LANF as a rising high P_f pulse reaches the fault core. Same notation as for Fig. 8. (a) The high P_f pulse has now migrated to the low angle normal fault core, and the anisotropy of cracks and pores promotes a permeability anisotropy, leading to increased fluid flow along the fault core. (b) A large increase in P_f in the foliated anisotropic core rocks can shift the stress state towards tensile failure, because σ_d is so reduced. (c) Waning P_f in the footwall with vertically oriented anisotropy leads to a reduction in σ_d and moves these rocks away from shear failure. (d) The hanging wall is still protected from changes in P_f by the fault core, and the stress state barely changes.

LANFs, but in most cases the earlier history of the fault is associated with fluids derived from deeper metamorphic or igneous sources, and the shallower fluid signal is imposed later as the fault system is exhumed to the surface (Kerrich, 1986; Wickham et al., 1993; Smith et al., 2008b).

7. Discussion

7.1. Pore pressure/stress coupling and anisotropy

The predicted (and counterintuitive) effects of pore fluid pressure changes on the effective stress, described in Section 3, can be linked to observations from hydrocarbon reservoirs (Teufel et al., 1991). Depletion in these reservoirs through the extraction of oil or gas has produced measurable drops in both P_f and the minimum horizontal stress (s_h), while overpressures or fluid injection show coupled increases of these values. Data from several basins and reservoirs suggest an average ratio for the coupling of s_h with P_f of ~70% (Hillis, 2000). This pore pressure/stress coupling has been explained by uniaxial compaction and isotropic poroelasticity (Engelder and Fischer, 1994), but given the ubiquity of saturated crack damage in the upper crust (Crampin and Chastin, 2003) and the behaviour described in Section 3, anisotropic poroelasticity may be more relevant (Chen and Nur, 1992).

7.2. Stress rotations and LANFs

For the stress rotation model to apply to the nucleation of LANFs, the layers or zones of altered elastic properties need to be inclined to the orientation of σ_1. The ubiquity of dipping contacts in natural settings is obvious, and the existence of any perfectly horizontal layering oriented perpendicular to a vertical σ_1 is highly unlikely. The stress rotation model of Casey (1980) provides a simple yet powerful framework to describe the nucleation of LANFs: nucleation occurs when layers with distinctly weaker material properties, whether anisotropic or isotropic, dip with respect to the imposed maximum compression. Such a rotation of σ_1 is enhanced by increased pore fluid pressures and additional extrinsic anisotropy (Fig. 7).

The model presented in this paper centres on LANFs with foliated, anisotropic cores. Many LANFs, particularly the detachment faults in the core complexes of the Western USA, lack foliated fault core rocks (Davis et al., 1980; Reynolds and Lister, 1987; Axen and Selverstone, 1994). The cores of these fault zones are dominated by chloritic gouges and breccias, and even those with significant clay content show little anisotropy (Haines et al., in press). Stress rotations are still possible in these granular quasi-isotropic fault rocks. As discussed in Section 5.2, cataclastic deformation can produce an increase in Poisson's ratio, and this will rotate σ_1 towards the fault core.

7.3. Fluids, seismicity and frictional sliding on LANFs

Forsyth (1992) pointed out that LANFs are more efficient in accommodating large displacements and Wernicke (1995) suggested that the earthquake recurrence interval of extensional faults is a function of their dip, and that LANF events could therefore be larger but much less common than HANF events. However, increased data collection has found interesting variations in the seismicity of active LANFs. The Woodlark detachment has experienced two large events ($M_W = 6.2$ and 6.8) in a fifteen-year interval (Abers et al., 1997). In contrast, the Alto Tiberina fault (ATF) in central Italy experiences ~3 small events ($M_L < 2.3$) per day (Chiaraluce et al., 2007) and a possible LANF beneath Corinth in Greece experienced 8 small events ($M < 3$) in 2 months during 1991 (Rietbrock et al., 1996). These observations are obviously a function of the time spent collecting the data and the level of instrumentation deployed, but there is an apparently large range in the seismic behaviour of LANFs.

In the model developed in Section 6, the possibility of frictional slip events on an LANF is restricted to the time interval immediately following tensile failure in the fault core. A large drop in P_f,

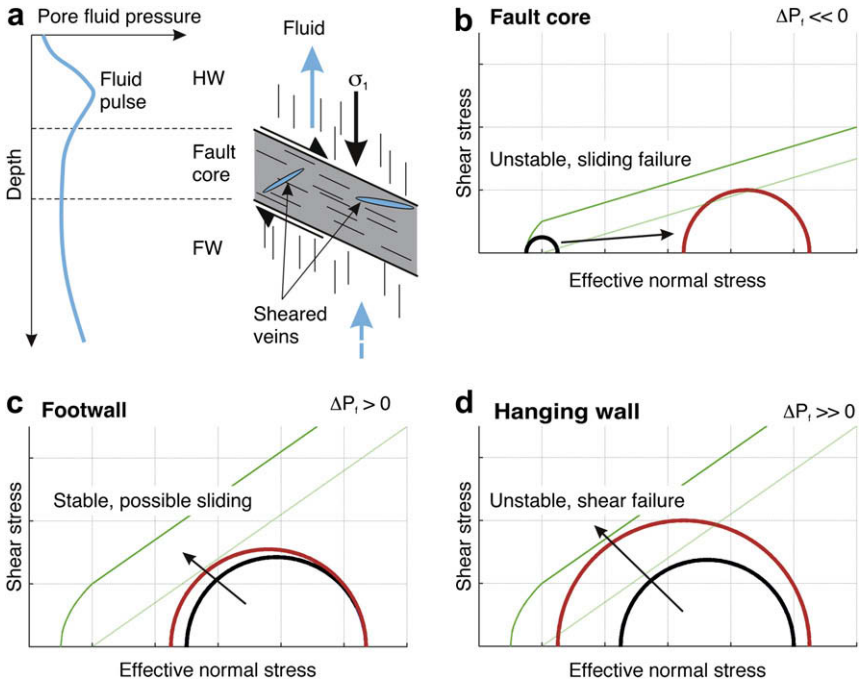

Fig. 10. Stress states in and around a LANF as a rising high P_f pulse reaches the hanging wall. Same notation as for Fig. 8. (a) Tensile hydrofracture veins in the fault core will now be deformed and rotated into concordance with the fault fabric, as the fluid is released into the HW. (b) Tensile failure in the fault core and the subsequent loss of P_f could push the stress state back towards frictional sliding. Seismicity in the fault core may therefore follow, and be a consequence of, hydrofracture. (c) As the next fluid pulse builds from below, a rise in P_f will again destabilise the FW, promoting further HANFs. (d) Increased P_f in the HW with vertical crack damage generates an increase in σ_d and the possibility of sliding on existing HANFs or shear failure to form new HANFs.

combined with the effects of anisotropy discussed in Section 3, can push the stress state back towards the frictional sliding envelope. The magnitude of this increase in σ_d within the anisotropic fault core is the key factor governing any seismic (frictional) slip, and this depends on the intrinsic anisotropy (i.e. the lithology, see Fig. 6) and the extrinsic anisotropy (i.e. the magnitude of crack damage, see Fig. 5). Serpentinites in the Woodlark detachment fault core can sustain a higher degree of σ_d for a given level of damage (Fig. 6b) compared to either shale or schist (Fig. 6a and c), assuming the elasticity values in Table 1 are relevant. As pore fluid pressure wanes after tensile failure events, these differences in σ_d could generate very different magnitudes of seismic slip in the core. Rapid recovery of high σ_d in the serpentinite dominated fault core of the Woodlark is consistent with large seismic events as the stress state meets the frictional sliding envelope at high effective stresses. In contrast, most of the fault core of the ATF lies within phyllitic rocks (Collettini and Barchi, 2002; their Fig. 8), which may be closer in elastic properties to shales and schists, and this would promote smaller seismic events at lower σ_d.

Not all LANFs display evidence for tensile hydrofractures e.g. Death Valley detachments have few syntectonic veins, but carry abundant evidence for hydrous authigenic minerals in the fault core zone (Cowan et al., 2003; Hayman, 2006). If a large fraction of any free fluid phase can be incorporated into the lattice structure of new minerals growing in the fault core, and at a rate quick enough with respect to the imposed strain rate, this might also serve to reduce the potential for seismic slip (Cowan et al., 2003).

8. Summary

The model for LANFs presented in this paper is based on the observation of anisotropy in the foliated and saturated core rocks of many LANFs. This anisotropy is due to the preferred orientations of phyllosilicates and parallel cracks and grain boundary pores. In the absence of measurements of elastic stiffness from natural shallow crustal fault rocks, this anisotropy can be quantified using the theoretically robust and experimentally validated EMT. Anisotropy in the fault core combines with pore fluid pressure changes, and leads to counterintuitive results for effective stresses. This anisotropic poroelastic model adds a micromechanical dimension to the established isotropic poroelastic model (Rice, 1992; Axen, 1992), and is rooted in measurable changes to rock properties. At a larger scale, the model can explain the common association of LANFs with HANFs, elevated pore fluid pressures and widely varying degrees of seismicity.

Acknowledgements

The author would like to thank Curtin University undergraduate students of GEOL207/241 (2008 cohort) for asking Why? during the class on Mohr circles, Joel Sarout for preprints and clarification and Curtin University for funding a TIGeR Fellowship. Steve Smith, Heather Sheldon and Rob Westaway are all thanked for comments. Detailed and constructive reviews by Yves Guéguen and Gary Axen helped to clarify and balance the arguments made in this paper. Tom Blenkinsop is thanked for prompt editorial handling. This is TIGeR publication 175.

References

Abers, G.A., 1991. Possible seismogenic shallow-dipping normal faults in the Woodlark-D'Entrecasteaux extensional province, Papua New Guinea. Geology 19 (12), 1205–1208.

Abers, G.A., Mutter, C.Z., Fang, J., 1997. Shallow dips of normal faults during rapid extension: earthquakes in the Woodlark-D'Entrecasteaux rift system, Papua New Guinea. Journal of Geophysical Research 102, 15301–15317.

Andreani, M., Mével, C., Boullier, A.M., Escartín, J., 2007. Dynamic control on serpentine crystallization in veins: constraints on hydration processes in oceanic peridotites. Geochemistry Geophysics Geosystems 8 (2).

Axen, G.J., 1992. Pore pressure, stress increase, and fault weakening in low-angle normal faulting. Journal of Geophysical Research 97 (B6), 8979–8991.
Axen, G.J., 1999. Low-angle normal fault earthquakes and triggering. Geophysical Research Letters 26 (24), 3693–3696.
Axen, G.J., Selverstone, J., 1994. Stress state and fluid-pressure level along the Whipple detachment fault, California. Geology 22 (9), 835–838.
Ayling, M.R., Meredith, P.G., Murrell, S.A.F., 1995. Microcracking during triaxial deformation of porous rocks monitored by changes in rock physical properties, I. Elastic-wave propagation measurements on dry rocks. Tectonophysics 245 (3–4), 205–221.
Brace, W.F., Paulding Jr., B.W., Scholz, C., 1966. Dilatancy in the fracture of crystalline rocks. Journal of Geophysical Research 71.
Bradshaw, G.A., Zoback, M.D., 1988. Listric normal faulting, stress refraction, and the state of stress in the Gulf-Coast Basin. Geology 16 (3), 271–274.
Byerlee, J., 1978. Friction of rocks. Pure and Applied Geophysics 116 (4), 615–626.
Carroll, M.M., 1979. An effective stress law for anisotropic elastic deformation. Journal of Geophysical Research 84 (B13), 7510–7512.
Casey, M., 1980. Mechanics of shear zones in isotropic dilatant materials. Journal of Structural Geology 2 (1–2), 143–147.
Chen, Q., Nur, A., 1992. Pore fluid pressure effects in anisotropic rocks: mechanisms of induced seismicity and weak faults. Pure and Applied Geophysics 139 (3), 463–479.
Chester, F.M., Friedman, M., Logan, J.M., 1985. Foliated cataclasites. Tectonophysics 111 (1–2), 139–146.
Chiaraluce, L., Chiarabba, C., Collettini, C., Piccinini, D., Cocco, M., 2007. Architecture and mechanics of an active low-angle normal fault: Alto Tiberina fault, northern Apennines, Italy. Journal of Geophysical Research 112 (B10), 10310, doi:10.1029/2007JB005015.
Chiodini, G., Frondini, F., Cardellini, C., Parello, F., Peruzzi, L., 2000. Rate of diffuse carbon dioxide earth degassing estimated from carbon balance of regional aquifers: the case of central Apennine, Italy. Journal of Geophysical Research – Solid Earth 105 (B4), 8423–8434.
Collettini, C., Barchi, M.R., 2002. A low-angle normal fault in the Umbria region (Central Italy): a mechanical model for the related microseismicity. Tectonophysics 359 (1–2), 97–115.
Collettini, C., Holdsworth, R.E., 2004. Fault zone weakening and character of slip along low-angle normal faults: insights from the Zuccale fault, Elba, Italy. In: Geological Society of London, vol. 161 pp.1039–51.
Collettini, C., De Paola, N., Goulty, N.R., 2006. Switches in the minimum compressive stress direction induced by overpressure beneath a low-permeability fault zone. Terra Nova 18 (3), 224–231.
Cowan, D.S., Cladouhos, T.T., Morgan, J.K., 2003. Structural geology and kinematic history of rocks formed along low-angle normal faults, Death Valley, California. Bulletin of the Geological Society of America 115 (10), 1230–1248.
Crampin, S., Chastin, S., 2003. A review of shear wave splitting in the crack-critical crust. Geophysical Journal International 155 (1), 221–240.
Davis, G.A., Andersson, J.L., Frost, E.G., Shackelford, T.J., 1980. Mylonitization and detachment faulting in the Whipple–Buckskin–Rawhide Mountains terrane, southeastern California and western Arizona. In: Geological Society of America Memorials, vol. 153, pp. 79–129.
Dewhurst, D.N., Brown, K.M., Clennell, M.B., Westbrook, G.K., 1996. A comparison of the fabric and permeability anisotropy of consolidated and sheared silty clay. Engineering Geology 42 (4), 253–267.
Dewhurst, D.N., Siggins, A.F., 2006. Impact of fabric, microcracks and stress field on shale anisotropy. Geophysical Journal International 165 (1), 135–148.
Engelder, T., Fischer, M.P., 1994. Influence of poroelastic behavior on the magnitude of minimum horizontal stress, Sh, in overpressured parts of sedimentary basins. Geology 22 (10), 949–952.
Famin, V., Nakashima, S., 2005. Hydrothermal fluid venting along a seismogenic detachment fault in the Moresby rift (Woodlark Basin, Papua New Guinea). Geochemistry Geophysics Geosystems 6.
Faulkner, D.R., Mitchell, T.M., Healy, D., Heap, M.J., 2006. Slip on 'weak' faults by the rotation of regional stress in the fracture damage zone. Nature 444 (7121), 922–925.
Flinn, D., 1977. Transcurrent faults and associated cataclasis in Shetland. Journal of Geological Society 133 (3), 231.
Floyd, J.S., Mutter, J.C., Goodliffe, A.M., Taylor, B., 2001. Evidence for fault weakness and fluid flow within an active low-angle normal fault. Nature 411 (6839), 779–783.
Forsyth, D.W., 1992. Finite extension and low-angle normal faulting. Geology 20 (1), 27–30.
Fortin, J., Guéguen, Y., Schubnel, A., 2007. Effects of pore collapse and grain crushing on ultrasonic velocities and Vp/Vs. Journal of Geophysical Research 112 (B8).
Godfrey, N.J., Christensen, N.I., Okaya, D.A., 2000. Anisotropy of schists: contribution of crustal anisotropy to active source seismic experiments and shear wave splitting observations. Journal of Geophysical Research 105 (B12), 27991–28007.
Gratier, J.P., Renard, F., Labaume, P., 1999. How pressure solution creep and fracturing process interact in the upper crust to make it behave in both a viscous and brittle manner. Journal of Structural Geology 21, 1189–1197.
Guéguen, Y., Sarout, J., 2009. Crack-induced anisotropy in crustal rocks: predicted dry and fluid-saturated Thomsen's parameters. Physics of the Earth and Planetary Interiors.
Haines, S.H., van der Pluijm, B.A., Ikari, M.J., Saffer, D.M., Marone, C., in press. Clay fabric intensity in natural and artificial fault gouges: implications for brittle fault zone processes and sedimentary basin clay fabric evolution. Journal of Geophysical Research, doi:10.1029/2008JB005866.
Hayman, N.W., 2006. Shallow crustal fault rocks from the Black Mountain detachments, Death Valley, CA. Journal of Structural Geology 28 (10), 1767–1784.
Hayman, N.W., Knott, J.R., Cowan, D.S., Nemser, E., Sarna-Wojcicki, A.M., 2003. Quaternary low-angle slip on detachment faults in Death Valley, California. Geology 31 (4), 343–346.
Healy, D., Jones, R.R., Holdsworth, R.E., 2006a. Three-dimensional brittle shear fracturing by tensile crack interaction. Nature 439, 64–67.
Healy, D., Jones, R.R., Holdsworth, R.E., 2006b. New insights into the development of brittle shear fractures from a 3D numerical model of microcrack interaction. Earth and Planetary Science Letters 249, 14–28.
Healy, D., 2008. Damage patterns, stress rotations and pore fluid pressures in strike–slip fault zones. Journal of Geophysical Research 113, B12407, doi:10.1029/2008JB005655.
Hillis, R.R., 2000. Pore pressure/stress coupling and its implications for seismicity. Exploration Geophysics 31, 448–454.
Hirose, T., Bystricky, M., 2007. Extreme dynamic weakening of faults during dehydration by coseismic shear heating. Geophysical Research Letters 34 (14).
Jaeger, J.C., Cook, N.G.W., Zimmerman, R.W., 2007. Fundamentals of Rock Mechanics. Blackwell Publishing.
Jones, T., Nur, A., 1982. Seismic velocity and anisotropy in mylonites and the reflectivity of deep crustal fault zones. Geology 10 (5), 260–263.
Kachanov, M., 1993. On the effective moduli of solids with cavities and cracks. International Journal of Fracture 59 (1), R17–R21.
Katz, O., Reches, Z., 2004. Microfracturing, damage, and failure of brittle granites. Journal of Geophysical Research 109.
Keller, J.V.A., Pialli, G., 1990. Tectonics of the Island of Elba: a reappraisal. Bollettino della Società Geologica Italiana 109, 413–425.
Kerrich, R., 1986. Fluid infiltration into fault zones: chemical, isotopic, and mechanical effects. Pure and Applied Geophysics 124 (1), 225–268.
Kern, H., Wenk, H.R., 1990. Fabric-related velocity anisotropy and shear wave splitting in rocks from the Santa Rosa mylonite zone, California. Journal of Geophysical Research 95 (B7), 11213–11223.
Kopf, A., 2001. Permeability variation across an active low-angle detachment fault, western Woodlark Basin (ODP Leg 180) and its implication for fault activation. In: Geological Society of London Special Publications, vol. 186(1), pp. 23.
Kopf, A., Behrmann, J.H., Deyhle, A., Roller, S., Erlenkeuser, H., 2003. Isotopic evidence (B, C, O) of deep fluid processes in fault rocks from the active Woodlark Basin detachment zone. Earth and Planetary Science Letters 208 (1–2), 51–68.
Lachenbruch, A.H., 1980. Frictional heating, fluid pressure, and the resistance to fault motion. Journal of Geophysical Research 85 (B11).
Moore, D.E., Rymer, M.J., 2007. Talc-bearing serpentinite and the creeping section of the San Andreas fault. Nature 448 (7155), 795–797.
Numelin, T., Marone, C., Kirby, E., 2007. Frictional properties of natural fault gouge from a low-angle normal fault, Panamint Valley, California. Tectonics 26 (2).
Nye, J.F., 1985. Physical Properties of Crystals: Their Representation by Tensors and Matrices. Oxford University Press.
Rabbel, W., Beilecke, T., Bohlen, T., Fischer, D., Frank, A., Hasenclever, J., Borm, G., Kuck, J., Bram, K., Druivenga, G., Smithson, S., 2004. Super-deep vertical seismic profiling at the KTB deep drill hole (Germany): seismic close-up view of a major thrust zone down to 8.5 km depth. Journal of Geophysical Research – Solid Earth 109.
Reynolds, S.J., Lister, G.S., 1987. Structural aspects of fluid-rock interactions in detachment zones. Geology 15 (4), 362–366.
Rice, J.R., 1992. Fault stress states, pore pressure distributions, and the weakness of the San Andreas fault. In: Evans, B., Wong, T.-F. (Eds.), Fault Mechanics and Transport Properties in Rocks. Academic Press, pp. 475–503.
Rietbrock, A., Tiberi, C., Scherbaum, F., Lyon-Caen, H., 1996. Seismic slip on a low angle normal fault in the Gulf of Corinth: evidence from high-resolution cluster analysis of microearthquakes. Geophysical Research Letters 23 (14), 1817–1820.
Roller, S., Behrmann, J.H., Kopf, A., 2001. Deformation fabrics of faulted rocks, and some syntectonic stress estimates from the active Woodlark Basin detachment zone. In: Geological Society of London Special Publications, vol. 187(1), pp. 319.
Rutter, E.H., Maddock, R.H., Hall, S.H., White, S.H., 1986. Comparative microstructures of natural and experimentally produced clay-bearing fault gouges. Pure and Applied Geophysics 124 (1), 3–30.
Sarout, J., Guéguen, Y., 2008. Anisotropy of elastic wave velocities in deformed shales: part 2 – modeling results. Geophysics 73, D91.
Sayers, C.M., Kachanov, M., 1995. Microcrack induced elastic-wave anisotropy of Brittle rocks. Journal of Geophysical Research – Solid Earth 100 (B3), 4149–4156.
Schubnel, A., Nishizawa, O., Masuda, K., Lei, X.J., Xue, Z., Guéguen, Y., 2003. Velocity measurements and crack density determination during wet triaxial experiments on Oshima and Toki granites. Pure and Applied Geophysics 160 (5), 869–887.
Schubnel, A., Benson, P.M., Thompson, B.D., Hazzard, J.F., Young, R.P., 2006. Quantifying damage, saturation and anisotropy in cracked rocks by inverting elastic wave velocities. Pure and Applied Geophysics 163 (5), 947–973.
Scott, T.E., Ma, Q., Roegiers, J.C., 1993. Acoustic velocity changes during shear enhanced compaction of sandstone. International Journal of Rock Mechanics and Mining Sciences & Geomechanics Abstracts 30 (7), 763–769.
Sibson, R.H., 1992. Implications of fault-valve behavior for rupture nucleation and recurrence. Tectonophysics 211 (1–4), 283–293.
Smith, S.A.F., Holdsworth, R.E., Collettini, C., Imber, J., 2007. Using footwall structures to constrain the evolution of low-angle normal faults. Journal of the Geological Society 164 (6), 1187.

Smith, S.A.F., Collettini, C., Holdsworth, R.E., 2008a. Recognizing the seismic cycle along ancient faults: CO_2-induced fluidization of breccias in the footwall of a sealing low-angle normal fault. Journal of Structural Geology.

Smith, S.A., Holdsworth, R.E., Collettini, C., MacPherson, C.G., Pearce, M.A., Faulkner, D., 2008b. The nature and evolution of fluid-related weakening mechanisms along a continental low-angle normal fault: the Zuccale fault, Elba Island, Italy. Eos Trans. AGU, 89(53) Fall Meet. Suppl, Abstract T21D-02.

Song, I., Suh, M., Woo, Y.K., Hao, T., 2004. Determination of the elastic modulus set of foliated rocks from ultrasonic velocity measurements. Engineering Geology 72 (3–4), 293–308.

Taylor, B., Huchon, P., 2002. Active continental extension in the western Woodlark Basin: a synthesis of Leg 180 results. Proceedings of the ODP, Scientific Results 180.

Teufel, L.W., Rhett, D.W., Farrell, H.P., 1991. Effect of reservoir depletion and pore pressure draw-down on in situ stress and deformation in the Ekofisk field, North Sea. In: Roegiers, J.C. (Ed.), Rock Mechanics as a Multidisciplinary Science. Balkema, Rotterdam, pp. 63–72.

Townend, J., Zoback, M.D., 2004. Regional tectonic stress near the San Andreas fault in central and southern California. Geophysical Research Letters 31.

Valcke, S.L.A., Casey, M., Lloyd, G.E., Kendall, J.M., Fisher, Q.J., 2006. Lattice preferred orientation and seismic anisotropy in sedimentary rocks. Geophysical Journal International 166 (2), 652–666.

Vernik, L., 1994. Hydrocarbon generation induced microcracking of source rocks. Geophysics 59.

Vernik, L., Liu, X., 1997. Velocity anisotropy in shales: a petrophysical study. Geophysics 62.

Wang, C.Y., Mao, N.H., Wu, F.T., 1979. The mechanical property of montmorillonite clay at high pressure and implications on fault behavior. Geophysical Research Letters 6 (6).

Watanabe, T., Kasami, H., Ohshima, S., 2007. Compressional and shear wave velocities of serpentinized peridotites up to 200 MPa. Earth, Planets, and Space 59 (4), 233–244.

Wernicke, B., 1995. Low-angle normal faults and seismicity: a review. Journal Of Geophysical Research 100, 20.

Westaway, R., 1999. The mechanical feasibility of low-angle normal faulting. Tectonophysics 308 (4), 407–443.

Westaway, R., 2005. Active low-angle normal faulting in the Woodlark extensional province, Papua New Guinea: a physical model. Tectonics 24 (6).

Wibberley, C.A.J., Shimamoto, T., 2005. Earthquake slip weakening and asperities explained by thermal pressurization. Nature 436 (7051), 689–692.

Wibberley, C.A.J., Yielding, G., Di Toro, G., 2008. Recent advances in the understanding of fault zone internal structure: a review. In: Geological Society of London Special Publications, vol. 299, pp. 5–33.

Wickham, S.M., Peters, M.T., Fricke, H.C., O'Neil, J.R., 1993. Identification of magmatic and meteoric fluid sources and upward-and downward-moving infiltration fronts in a metamorphic core complex. Geology 21 (1), 81–84.

Zoback, M.D., Zoback, M.L., Mount, V.S., Suppe, J., Eaton, J.P., Healy, J.H., Oppenheimer, D., Reasenberg, P., Jones, L., Raleigh, C.B., 1987. New evidence on the state of stress of the San Andreas fault system. Science 238, 1105–1111.